Chapter 5
Lightning Analysis of Wind Turbines

Yeqing Wang

5.1 Introduction

5.1.1 Basic Physics of Lightning Strikes

Lightning discharge is essentially the dielectric breakdown of the air. It occurs when the strength of the electric field between the cloud and the earth or between two clouds exceeds the dielectric breakdown strength of the air (i.e., 3 MV/m). Due to the large intensity of the electric field, the air molecules are ripped apart, leaving free electrons and positive ions. Meanwhile, the electric field between the cloud and the earth or between two clouds accelerates these charges causing a rapid motion of the electric charge, which heats the surrounding air molecules up to 50,000 °F (i.e., almost five times the temperature of the Sun's surface) (Oard 2015). The extreme heat leads to a rapid volume expansion of the air and, thus, emanates sound waves (i.e., the thunder). In addition to the sound waves, the lightning plasma channel also emits light, radio waves, x-rays, and even gamma rays (Rupke 2002).

The luminous lightning flash (i.e., can be visually observed in the air) is not instantly formed after the dielectric breakdown of the air. Instead, a few steps with durations of several milliseconds are completed prior to the formation of the luminous lightning flash. Taking the negative polarity downward initiated cloud-to-ground (CG) lightning flash for example, in the beginning of the lightning flash, the positive charge in the cloud travels in the speed of light through the air

Y. Wang (✉)
Department of Mechanical and Aerospace Engineering, University of Florida, Gainesville, FL, USA
e-mail: yeqwang@reef.ufl.edu

W. Hu (ed.), *Advanced Wind Turbine Technology*,
https://doi.org/10.1007/978-3-319-78166-2_5

propagating toward the ground. The propagating channel, known as the lightning stepped leader, is a weakly luminous channel that can be visually observed in the air and only lasts for several milliseconds. As the lightning stepped leader approaches the ground, the intensified electric field between the tip of the lightning stepped leader and the ground structures triggers the ground structures to emit answering leaders. Once the lightning stepped leader connects with the answering leader, the first luminous lightning channel, known as the lightning return stroke (i.e., the channel with negative charge that travels from the ground to the cloud), is then formed. Common structures that can emit answering leaders are normally electrically conductive such as transmission towers and TV towers. Moreover, the electrically non-conductive structures (e.g., glass fiber-reinforced polymer-matrix (GFRP) composite wind turbine blades) are also able to emit answering leaders if conductive components (receptors and down conductors, etc.) or conductive contamination (salt, dirt, moisture, etc.) is included (Madsen 2006).

Furthermore, a typical lightning discharge includes one or more intermittent partial discharges; each component discharge is called a stroke. Figure 5.1 shows a standard waveform of the lightning strike electric current used for common lightning strike analysis, where the waveform components A, B, C, and D denote the initial return stroke, intermediate stroke, continuing stroke, and restrike stroke, respectively. The initial return stroke current has a pulsed profile with a peak reaching up to hundreds kiloamperes. The electric current return stroke wave heats and pressurizes the lightning plasma channel which leads to the rapid channel expansion, optical radiation, and shock wave propagation in the outward direction. The initial return stroke with high-intensity short-duration pulsed current is typically followed by a continuing stroke with almost constant current, which is about two orders of magnitude lower and three orders of magnitude longer than that of the pulsed current of the initial return stroke.

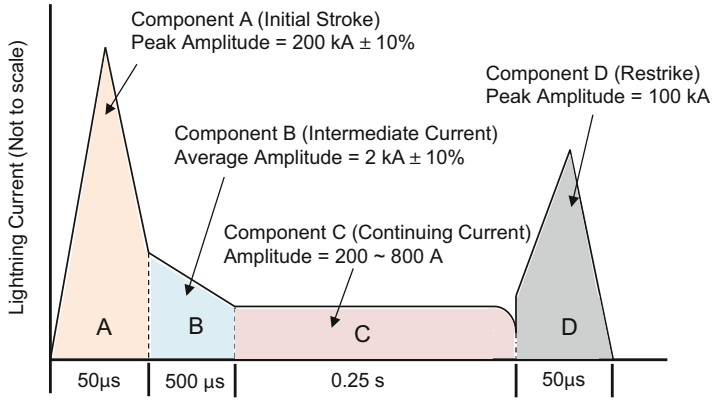

Fig. 5.1 Standard lightning current waveform suggested by MIL-464-A (1997)

5.1.2 Direct Effects of Lightning Strikes on Wind Turbines

5.1.2.1 Dielectric Breakdown

Lightning strikes cause frequent structure damage to the wind turbines, especially to the wind turbine blades which are typically made of the sandwiched composite laminated panels. The most widely used type of composite materials on the wind turbine blades are the electrically non-conductive glass fiber-reinforced polymer-matrix (GFRP) composite laminates. During a lightning strike event, the electric field strength in the vicinity of the composite wind turbine blades significantly intensifies. If it exceeds the dielectric breakdown strength of the composite wind turbine blade, the dielectric breakdown occurs and, thus, may result in pin holes or punctures in the blades. Typically, the electrical field required to puncture a given thickness of glass fiber or aramid fiber composite is greater than that required to ionize a similar thickness of air due to the high porosity and inhomogeneity of the composite structure (Rupke 2002). The dielectric breakdown strength of the solid composite material is highly dependent on the thickness, temperature, humidity, and pressure. A detailed discussion of the dielectric breakdown strength of the composite wind turbine blade is provided in Sect. 5.2.4.

5.1.2.2 Surface Flashover

In the case when the electric field strength on the composite wind turbine blade is lower than its dielectric breakdown strength, the lightning arc automatically searches for the weakest spots (i.e., least resistant) to conduct the lightning electric current once it attaches to the surface of the non-conductive composite wind turbine blade. If the electric field strength exceeds the surface flashover field strength (i.e., lower than the dielectric breakdown strength), the conduction of the lightning current on the surface can be visually observed in a form of surface flashover (also known as streamers). Figure 5.2 shows an example of a surface flashover on a composite wind turbine blade surface caused by the lightning arc. The surface flashover produces extensive heat along the conducting path and, thus, may lead to appreciable thermal damage, such as skin peeling, burning, melting, and material vaporization.

5.1.2.3 Lightning Strike-Induced Localized Damage on Composite Wind Turbine Blades

The direct injection of the lightning arc channel onto the surface of the composite wind turbine blade produces extensive localized damage, such as melting or burning on the lightning attachment points, and mechanical damage due to magnetic force and acoustic shock wave. If the blade is made of electrically conductive material (e.g., carbon fiber polymer-matrix composite laminates), the conduction of the

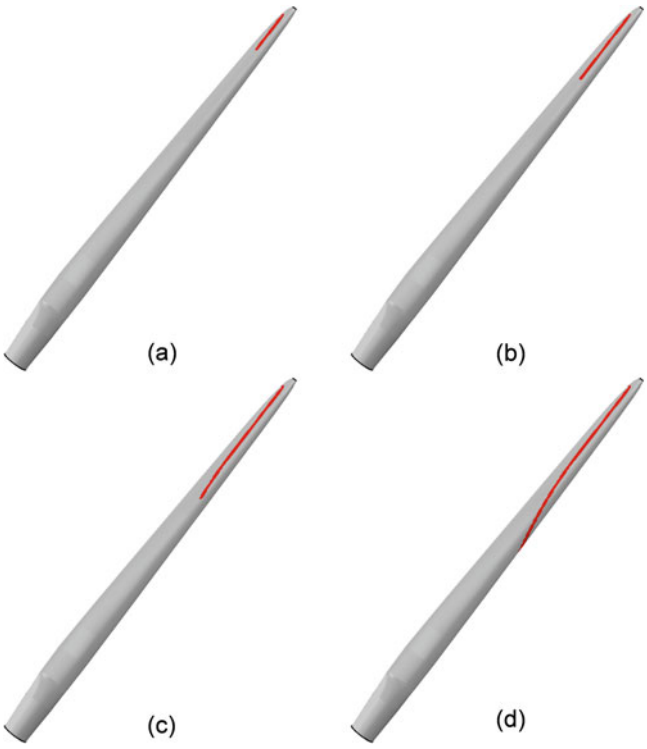

Fig. 5.2 Example of the evolution of the surface flashover on a wind turbine blade at 1 (**a**), 2 (**b**), 3 (**c**), and 4 milliseconds (**d**) (where the gray denotes room temperature and red denotes high temperatures)

lightning current through the interior of the conductive blade also produces extreme high Joule heating, which may lead to more extensive thermal damage. Generally, if a lightning arc attaches to the surface of the solid material, the direct heat flux injection leads to a rapid temperature rise on the surface of the composite wind turbine blade. With the increasing temperature, the resin component (i.e., the polymer matrix) of the composite material starts to decompose at around 300 °C and is fully consumed as the temperature reaches 800 °C. The decomposition of the resin leads to the fluctuations in the overall density and material properties of the material, the degradations in the material strength, and the liberation of the pyrolysis gases. The decomposition of the interlaminar resin will also lead to the delamination of the composite laminates. At temperatures around 1100 °C (or higher), the glass fiber quickly melts and vaporizes (or experiences rapid melt expulsion).

In addition, the pyrolysis gases may be trapped in between the laminate layers as the interlaminar resin decomposes. With the accumulation of the trapped pyrolysis gases, the volume of the pyrolysis gases expands, and if the stress caused by the internal pressure of the pyrolysis gases exceeds the rupture strength of the

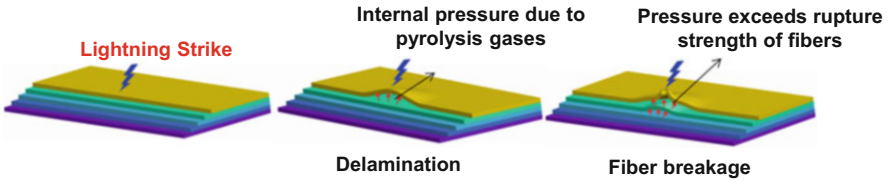

Fig. 5.3 Lightning-induced delamination and fiber breakage in polymer-matrix composite structures

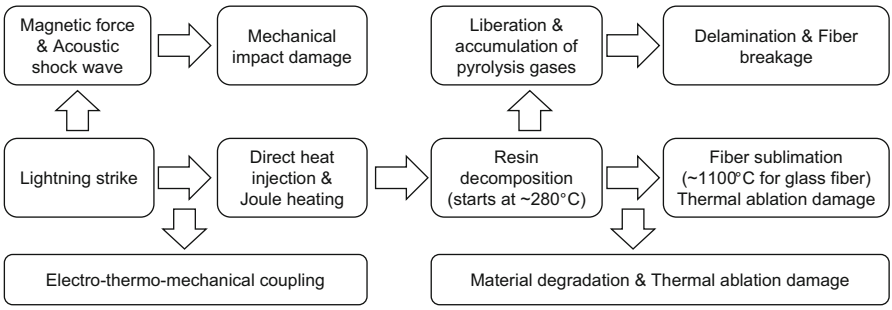

Fig. 5.4 Lightning strike direct effects on polymer-matrix composite laminated structures

fibers, fiber breakage develops and results in surface cracks (see Fig. 5.3). Inoue et al. (2004) studied the relationship between the pressure rise inside a laminated composite panel and the energy of a spark arc that is enforced on the composite blade surface. It was reported that the internal pressure between the laminate layers is proportional to the arc energy. Furthermore, the induced magnetic force and acoustic shock wave as the lightning arc attaches to the surface of the composite wind turbine blade may also result in minor mechanical impact damage (Chemartin et al. 2012; Muñoz et al. 2014). An overview of the lightning strike direct effects on polymer-matrix composite laminates is provided in Fig. 5.4.

5.1.3 Common Lightning Strike Protections (LSP) for Wind Turbines

As described in Sect. 5.1.1, the approaching of the lightning stepped leader toward the ground intensifies the electric field between the tip of the lightning stepped leader and the ground structures. When the tip of the lightning stepped leader arrives within a certain distance (i.e., the lightning striking distance) to a ground structure, answering leaders will be emitted from the structure and attempt to arrest the lightning stepped leader. Once they are connected, the first lightning return stroke is formed. Normally, structures such as metallic conductors are able to emit answering

leaders (as conductors allow electric charges to move freely under lightning electric field). As described earlier, non-conductive structures such as the GFRP composite wind turbine blades are also able to emit answering leaders due to the presence of internal down conductors, receptors, and surface contaminations (e.g., moisture, dirt, and rain drops).

To intercept the lightning stepped leader and conduct the high-intensity lightning current safely to the ground, the wind turbine blades are normally designed with lightning strike protections (LSP). The most commonly used LSP system is to embed conductive (e.g., special tungsten alloy) receptors on the surfaces of wind turbine blades (IEC-61400-24 2002). These receptors are connected to down conductors (e.g., unshielded high-voltage cables) which are installed inside the blade shell extending from the root to the tip of the blade. The receptors are designed to intercept the lightning strokes and safely conduct the lightning current through the down conductors to the earth. The efficiency of LSP is expressed as a product of interception efficiency and sizing efficiency, where the interception efficiency refers to the ability of the receptors to intercept a lightning stroke, and the sizing efficiency refers to the ability of the LSP system to conduct the lightning current (IEC-61400-24 2002). The sizing efficiency can be increased by increasing the diameter of the down conductors, while the interception efficiency may be increased by using multiple receptors. The receptors often undergo partial evaporation with repeated lightning strikes. They need to be replaced after every several lightning strikes. Figure 5.5 shows an example of embedding multiple receptors on the surface of a 100-meter long wind turbine blade. Recently, Wang and Hu investigated the effects of five different configurations of receptors on the lightning strike protection of wind turbine blades (Wang and Hu 2017).

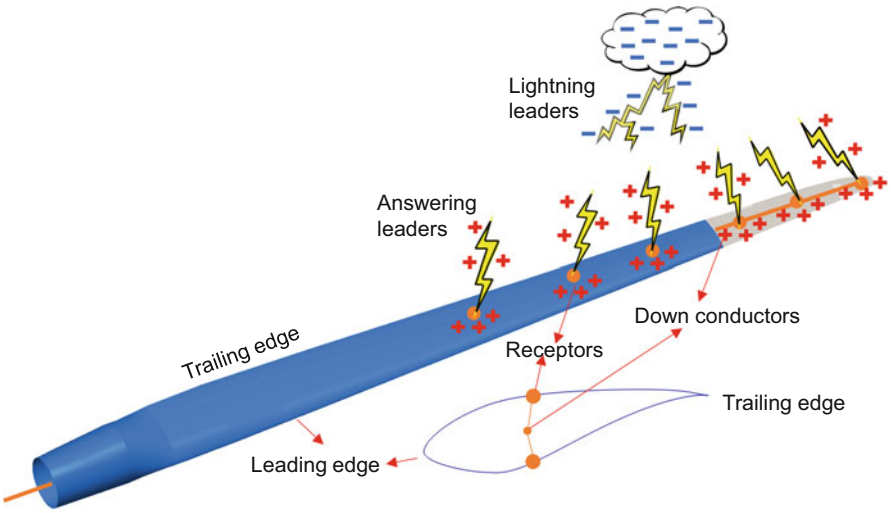

Fig. 5.5 A schematic of the formation of lightning leaders and answering leaders emitting from the receptors of a wind turbine blade

5.1.4 *Lightning Current Conduction on Electrically Non-conductive Composite Wind Turbine Blades*

Although LSP is widely used on wind turbines, lightning strike damage is still not completely avoidable. It has been reported that many electrically non-conductive wind turbine blades with the receptor and down conductor system are still subjected to lightning strike damage (Madsen 2006 and Madsen et al. 2006). This is because the answering leaders will not be only emitted from the receptors but will also be emitted from the non-conductive regions other than the receptors. If the emitted answering leaders from those non-conductive regions arrest the lightning stepped leader, appreciable thermal damage can occur due to the direct injection of the lightning arc. One prevalent hypothesis that explains the possible reason for the non-conductive regions on the blade surface to emit answering leaders is illustrated in the schematic diagram (see Fig. 5.6). It can be seen from Fig. 5.6, the large electric field due to the approaching of lightning stepped leader ionizes the molecules on the down conductor. Then, the ionized positive charges flow upward and deposit on the interior surface of the blade, which also induces negative charges on the exterior surface (see Fig. 5.6a). At the same time, the positive charges flow to the surface of the receptors and search for and neutralize those negative charges. The searching path through the electrically non-conductive blade regions can also emit multiple answering leaders (see Fig. 5.6b). If one of them arrests the approaching lightning stepped leader, the lightning arc channel is directly attached to the surface of the non-conductive blade region (see Fig. 5.6c), leading to a significant temperature increase and appreciable thermal damage on the attached spot. Moreover, severe damage, such as puncture through, can develop if the induced electric field strength at the attached spot exceeds the dielectric breakdown strength of the composite wind turbine blade (see Fig. 5.6d) (Madsen et al. 2006).

In general, if the lightning strike-induced electric field strength is lower than the dielectric breakdown strength of the GFRP composite wind turbine blade, the damage is predominately attributed to the direct heat conduction due to the lightning channel attachment on the surface of the structure. In contrast, if the electric field strength exceeds the dielectric breakdown strength of the GFRP composite wind turbine blade, the non-conductive blade becomes instantly conductive in the through-the-thickness direction, and a considerable amount of Joule heating will be produced along the conducting path. Once dielectric breakdown occurs, the Joule heating must be considered in the damage predictive models in addition to the direct heat conduction (i.e., radiative heat exchange between the lightning arc and the wind turbine blade). Therefore, an estimation of dielectric breakdown of the GFRP composite wind turbine blade subjected to a lightning stepped leader is essential and inevitable prior to any predictive lightning strike damage models of the non-conductive GFRP wind turbine blades. Section 5.2 introduces methods to predict the lightning strike-induced electric field strength and, hence, to estimate the dielectric breakdown of the GFRP composite wind turbine blade subjected to a lightning stepped leader.

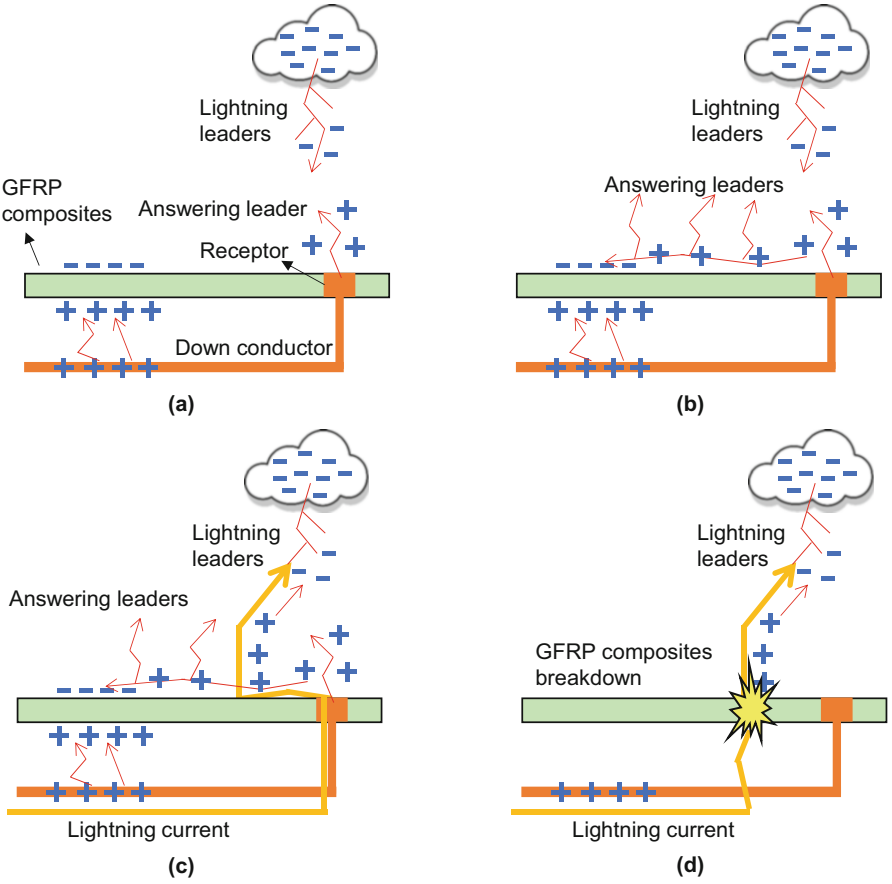

Fig. 5.6 Lightning attachment on a non-conductive surface: (**a**) free positive charges flow upward and deposit on the interior blade surface, inducing negative charges on the exterior blade surface; (**b**) positive charges on the receptor surface search for and neutralize negative charges on the exterior blade surface. Searching path and receptor emit answering leaders; (**c**) one of the answering leader emitted from the searching path captures the lightning stepped leader; (**d**) dielectric breakdown occurs when the electric field exceeds the dielectric breakdown strength of the blade

5.2 Analysis of Lightning Strike-Induced Electric Field at Wind Turbines

5.2.1 Lightning Striking Distance

As described in Sect. 5.1.1, the distance between the tip of the lightning stepped leader (i.e., the weakly luminous leader which propagates from the cloud to the ground) and the ground structure at the particular moment when the answering

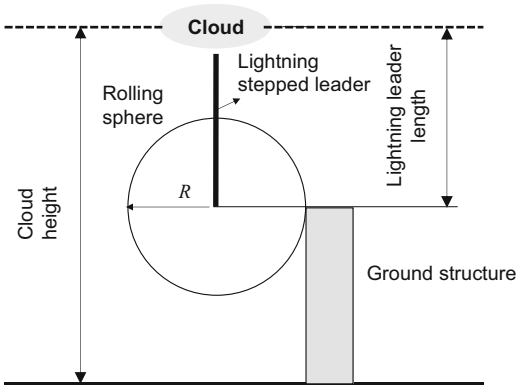

Fig. 5.7 Lightning striking distance from stepped leader tip to a ground structure characterized using the rolling sphere method

leaders are triggered from the ground structure is called the lightning striking distance. According to the IEC 61400–24 standard (IEC-61400-24 2002), for the wind turbine blades longer than 20 m, the lightning striking distance can be defined using the rolling sphere method, where the radius of the rolling sphere attached to the ground structure can be considered equal to the lightning striking distance (see Fig. 5.7).

The rolling sphere radius is a function of the peak current of the lightning return stroke. A traditional expression to calculate the sphere radius (and, therefore, the lightning striking distance) is given by Uman (2001):

$$R = 10 \cdot I_{\text{peak}}^{0.65}, \tag{5.1}$$

where I_{peak} is the peak current of the lightning return stroke (in kA), and R is the rolling sphere radius (in m).

Recently, Cooray et al. (2007) suggested another expression for the radius of the rolling sphere, which agrees better with the recorded physical measurement data on the lightning striking distances:

$$R = 1.9 \cdot I_{\text{peak}}^{0.90}, \tag{5.2}$$

where the rolling sphere radius R is in m and the unit of peak current I_{peak} is in kA. However, it should be noted that the above equation yields the lightning striking distance to a flat ground and not to an object protruding above the ground. Therefore, Eq. (5.2) may not be appropriate to be used to calculate the lightning striking distance to a wind turbine.

Another widely used equation for calculating the lightning striking distance is proposed by Eriksson (1979):

$$R = 0.6 \cdot I_{\text{peak}}^{1.46}, \tag{5.3}$$

Here, Eq. (5.3) is applicable for calculating the lightning striking distance to a wind turbine (Eriksson 1979).

Table 5.1 Lightning striking distance for the lightning stepped leader

LPL	Peak current, I_{peak} (kA)	Lightning striking distance (m)	
		From Eq. (5.1)	From Eq. (5.3)
I	200	313.09	1372.95
II	150	259.69	902.08
III	100	199.53	499.06

Table 5.1 shows the lightning striking distance calculated using Eqs. (5.1 and 5.3) for three lightning protection levels (LPLs). The LPLs represent three different lightning severity levels as identified by the IEC-61400-24 (2002). The peak current of the initial return strokes (see Fig. 5.1) is 200, 150, and 100 kA for LPL I, LPL II, and LPL III, respectively.

Table 5.1 shows that the lightning striking distances calculated by Eq. (5.3) are around 2.5 to 4 times larger than those calculated by Eq. (5.1). Therefore, using Eq. (5.3) may result in lower predictions of electric field strength at a ground structure, when compared to the predictions using Eq. (5.1).

As a side note, below we discuss the difference between the lightning striking distance and the lightning attractive radius, which are both widely used in the modeling of lightning attachment to structures.

The attractive radius can be calculated as (D'Alessandro and Petrov 2006):

$$R_a = 0.84 \cdot I_{\text{peak}}^{0.74} h_a^{0.6}, \tag{5.4}$$

where R_a is the attractive radius (in m), I_{peak} is the peak current (in kA), and h_a is the structure height (in m). There is a significant difference between lightning striking distance, R, as defined by Eqs. (5.1, 5.2 and 5.3), and the lightning attractive radius, R_a, as defined by Eq. (5.4). It can be noticed that the lightning striking distance depends on the charge transfer only, whereas the lightning attractive radius takes into account the size of the structure. Figure 5.8 shows the ratio R/R_a as a function of the structure height h_a for $I_{\text{peak}} = 100$ kA. For tall structures (i.e., $h_a > 35$ m), the lightning striking distance is smaller than the lightning attractive radius. Therefore, one needs to be cautious when choosing between the lightning striking distance and the lightning attractive radius for a conservative prediction of the lightning strike-induced electric field, since the results could be quite sensitive to the choice between the two.

5.2.2 Lightning Electric Charge Transfer

5.2.2.1 Charge Transfer of a Lightning Return Stroke

According to Cooray et al. (2007), as the lightning stepped leader approaches the ground, the charge density of the lightning stepped leader is determined by both

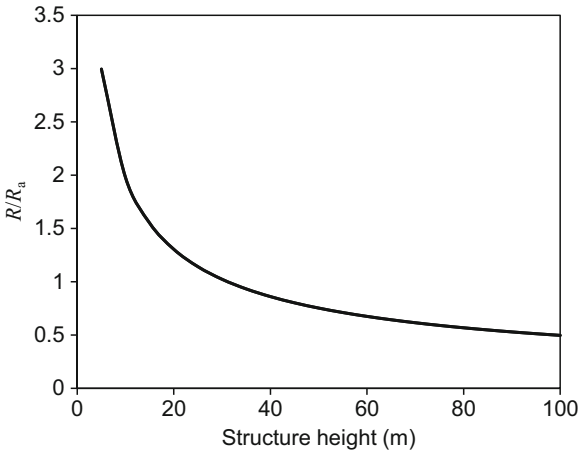

Fig. 5.8 Ratio of striking distance to the attractive radius as a function of the structure height ($I_{peak} = 100$ kA)

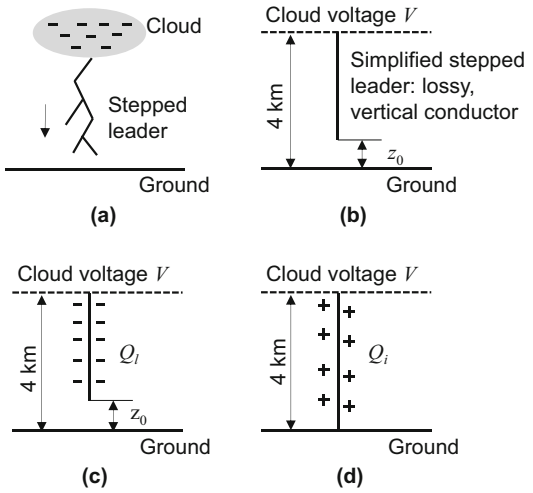

Fig. 5.9 Simplified lightning stepped leader model proposed by Cooray et al. (2007) (**a**) Real stepped leader (**b**) Simplified stepped leader (**c**) Negative charges on the stepped leader (**d**) Positive charges on the return stroke channel induced by the cloud voltage

the electric field due to the cloud charge and the electric field enhancement due to the presence of the ground. Figure 5.9 shows a simple lightning stepped leader model: a cloud is represented by a conductive plane at potential V, the ground is represented by a perfect conductor, and the lightning stepped leader is assumed to be a vertical line charge (where, in real situations, branched leaders may develop, and the weakly luminous paths of those leaders often form an inverted tree shape). Figure 5.9a shows a real lightning stepped leader approaching the ground with branched channels; Fig. 5.9b shows an idealized vertical lightning stepped leader; Fig. 5.9c shows a negative charge Q_l along the lightning stepped leader prior to the formation of the return stroke; Fig. 5.9d shows a positive charge Q_i flowing upward along the lightning channel that is induced by the cloud voltage after the initial return stroke is formed. The total positive charge, $Q_{t,\,100\mu s}$, entering from the

ground to the fully developed return stroke channel during the first 100 μs equals the sum of the positive charges that neutralize the negative charges Q_l stored along the lightning stepped leader and the positive charges Q_i due to the cloud voltage:

$$Q_{t,100\ \mu s} = |Q_l| + Q_i = 0.61 \cdot I_{\text{peak}}, \tag{5.5}$$

where $Q_{t,100\,\mu s}$ is in C, and I_{peak} is the peak current, in kA.

5.2.2.2 Charge Density of a Lightning Stepped Leader

Typically, the charge density of the lightning stepped leader is nonuniform (Becerra 2008; Cooray et al. 2007; Golde 1945, 1977; Lewke et al. 2007). Golde (1945, 1977) assumed that the charge density decreased exponentially along the lightning stepped leader from the tip to the origin of the leader in the cloud:

$$\lambda(\eta) = \lambda_0 e^{-\eta/\xi},\ \ 0 \le \eta \le L, \tag{5.6}$$

where λ is the charge density distribution (in C/m) along the leader; λ_0 is the charge density at the leader tip; ξ is the decay height constant, $\xi = 1000$ m; and L is the length of the leader (in m). In addition, $\eta = z\text{-}z_0$ (in m), where z is the vertical distance from the ground ($z = 0$ at the ground) and z_0 is the distance from the ground to the leader tip.

The total charge deposited on the leader is obtained by taking the integral of the charge density Eq. (5.6) over the leader length:

$$Q_l = \int_0^L \lambda(\eta)\, d\eta = \lambda_0 \xi \left[1 - e^{-L/\xi}\right], \tag{5.7}$$

where Q_l is the total charge (in C) (Golde 1945, 1977).

Meanwhile, the relationship between the peak current of the lightning return stroke and the charge density at the leader tip is

$$\lambda_0 = 4.36 \cdot 10^{-5} I_{\text{peak}}, \tag{5.8}$$

where I_{peak} is the peak current (in kA).

Using the charge simulation method, Cooray et al. (2007) derived a different nonuniform distribution for the charge density along the lightning stepped leader:

$$\begin{aligned} &\lambda(\eta) = a_0 \cdot \left(1 - \tfrac{\eta}{H - z_0}\right) \cdot G(z_0) \cdot I_{\text{peak}} + \tfrac{I_{\text{peak}} \cdot (a + b \cdot \eta)}{1 + c \cdot \eta + d \cdot \eta^2} \cdot F(z_0), \\ &\quad 0 \le \eta \le L,\ \ z_0 \ge 10, \end{aligned} \tag{5.9}$$

where η, in m, is the distance along the leader, $\eta = 0$ is at the leader tip, $\eta = z\text{-}z_0$, $\lambda(\eta)$ is the line charge density (in C/m), H is the height of the cloud (typically

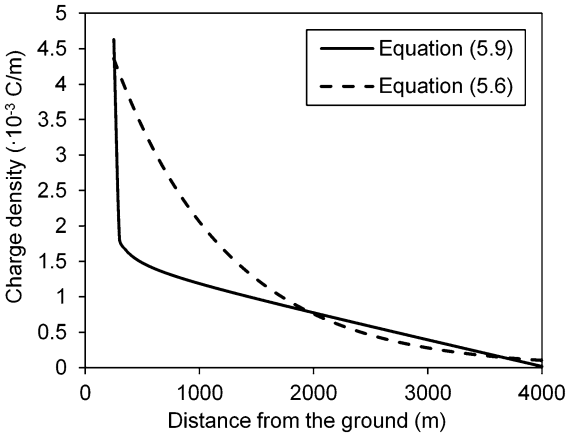

Fig. 5.10 Charge density of the lightning stepped leader for the LPL III (i.e., $I_{peak} = 100$ kA) (when $z_0 = 250$ m)

Table 5.2 Total charge entering from the ground to the lightning channel, $Q_{t,\,100\,\mu s}$, and the total charge deposited on the lightning stepped leader, Q_l

	$Q_{t,\,100\,\mu s}$ (C)		Q_l (C)	
LPL	From IEC-61400-24	From Eq. (5.5)	From Eq. (5.6)	Integral of Eq. (5.9)
I	300	183	8.51493	5.70252
II	225	91.5	6.38619	4.27689
III	150	61	4.25746	2.85126

$H = 4000$ m), z_0 is the distance from the ground to the leader tip (in m), I_{peak} is the peak current of the return stroke (in kA), and $G(z_0) = 1\text{-}(z_0/H)$, $F(z_0) = 0.3\alpha + 0.7\beta$, $\beta = 1\text{-}(z_0/H)$, $a_0 = 1.476 \times 10^{-5}$, $a = 4.857 \times 10^{-5}$, $b = 3.9097 \times 10^{-6}$, $c = 0.522$, and $d = 3.73 \times 10^{-3}$. It is assumed that $z_0 > 10$ m. Cooray et al. (2007) found that the distribution Eq. (5.9) was in a better agreement with the physical measurements than the distribution Eq. (5.6) proposed by Golde (1945, 1977). The total charge deposited on the leader is obtained by numerically taking the integral of the charge density Eq. (5.9) over the length of the leader.

Figure 5.10 shows the charge density as a function of the height z (i.e., distance from the ground). Calculations are performed using Eqs. (5.6 and 5.9) for the LPL III (i.e., $I_{peak} = 100$ kA). The distance from the stepped leader tip to the ground is $z_0 = 250$ m, and the length of the lightning stepped leader is $L = 3750$ m. As one can see, at the leader tip and at the vicinity of the cloud, the charge densities calculated by Eqs. (5.6 and 5.9) are similar, but they are quite different in between. Table 5.2 shows the total charge entering from the ground to the lightning channel, $Q_{t,100\,\mu s}$, within the first 100 μs, calculated using Eq. (5.5) and provided by the IEC 61400–24 standard (IEC-61400-24 2002), and the total charge on the leader, Q_l, in the case of uniform (5.6) and nonuniform (5.9) charge density distributions. As one can see, the total charge is larger if charge density is uniform. However, the charge density near the lightning stepped leader tip (i.e., the distance from the ground is around 250 m, see Fig. 5.10) is larger, if calculated using the charge density distribution (5.9).

5.2.3 *Prediction of Lightning Strike-Induced Electric Field in the Vicinity of a Wind Turbine: Analytical and Finite Element Methods*

In this section, we present two methods, the analytical and finite element methods (FEM), to predict the static electric field (i.e., the effects of the lightning stepped leader propagation are not considered) in the vicinity of a wind turbine induced by a lightning stepped leader. The first simple method provides a qualitative estimation of the electric field by using an analytical approach, while the second method incorporates the charge density (i.e., Eqs. (5.6 and 5.9)) into a finite element model with COMSOL, which provides more accurate predictions of the electric field.

5.2.3.1 Analytical Model

In this section, we assume the charge density of a lightning stepped leader to be uniform and calculate the induced electric field at the vertically positioned blade (i.e., blade *OA*, see Fig. 5.11). To simplify the problem, here, we make a few more assumptions: (i) the ground (i.e., zero electric potential) is at the infinity, (ii) the electric potential between a cloud and the ground is ignored, and (iii) the effects of the wind turbine receptors and down conductors on the electric fields are disregarded. With these assumptions, the problem of calculating the electric field due to a vertical lightning stepped leader becomes similar to calculations of the electric field due to a charged lines and rods (Tipler and Mosca 2007; Uman 2001).

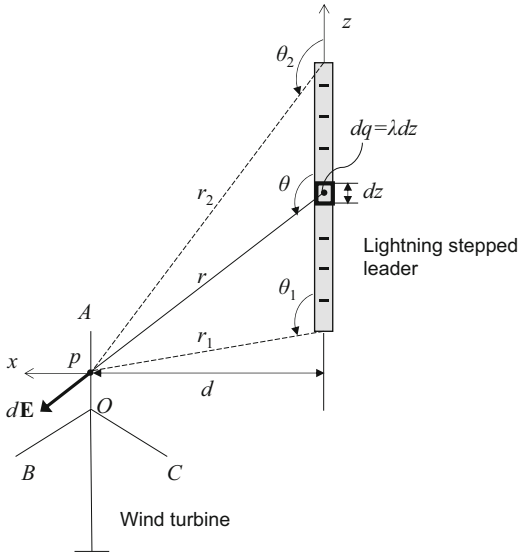

Fig. 5.11 Electric field calculation at point *p* of the blade *OA* due to a uniformly charged lightning stepped leader

As described in Sect. 5.2.2, the lightning stepped leader is assumed to be a vertical line charge with uniform charge density:

$$\lambda = \frac{Q_l}{L}. \tag{5.10}$$

where λ is the line charge density (in C/m), Q_l is the total charge (in C) deposited on the lightning stepped leader calculated by taking the integral of the nonuniform charge density Eq. (5.9), and L is the length of the lightning stepped leader (in m). The electric field due to a line charge can be calculated using the Coulomb's law based on the assumption that the field due to an infinitesimal line charge element dq is the same as the field due to a point charge. Therefore, the electric field at an arbitrary point p of the blade OA due to the charge dq within dz can be calculated as:

$$dE = \frac{kdq}{r^2} = \frac{k\lambda dz}{r^2} = \frac{k\lambda d\theta}{d}, \tag{5.11}$$

where r is the distance from the element charge dq to the point p at the blade, $k = 9 \times 10^9$ N·m^2·C^{-2} is Coulomb's constant, and $d = r \cdot \sin\theta$ is the lightning striking distance, which is equal to the rolling sphere radius (see discussions in Sect. 5.2.1). The x and z components of the electric field E from all the charge in the leader are

$$\begin{aligned} E_x &= \int_{\theta_1}^{\theta_2} \sin\theta \frac{k\lambda d\theta}{d} = -\frac{k\lambda}{d}\left(\cos\theta_2 - \cos\theta_1\right), \\ E_z &= \int_{\theta_1}^{\theta_2} \cos\theta \frac{k\lambda d\theta}{d} = \frac{k\lambda}{d}\left(\sin\theta_2 - \sin\theta_1\right). \end{aligned} \tag{5.12}$$

Finally, the magnitude (i.e., strength) of the electric field at a particular point p along the blade OA due to the lightning stepped leader is

$$|E| = \sqrt{E_x^2 + E_z^2} = \frac{2k\lambda}{d} \sin\frac{\theta_2 - \theta_1}{2}. \tag{5.13}$$

Here $|E|$ denotes the magnitude of the electric field (in V/m).

5.2.3.2 Finite Element Model

In this section, we present a finite element model to predict the electric field in the vicinity of a wind turbine due to a lightning stepped leader. The finite element analysis (FEA) is performed using the COMSOL Multiphysics®. This finite element model enables us to account for the effects of the nonuniform charge density distribution Eq. (5.9), the effects of the receptors and down conductors, and the finite ground that were not included in the analytical model considered in Sect. 5.2.3.1, which, therefore, provides us more accurate predictions.

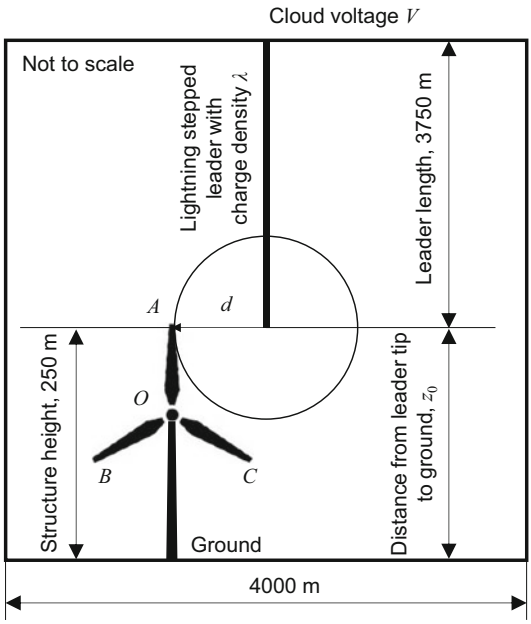

Fig. 5.12 Interaction of a lightning stepped leader and a wind turbine: problem formulation

In particular, we consider a horizontal axis wind turbine blade (see Fig. 5.12), the three blades of which are placed on top of a 150-m wind turbine tower, representing the Sandia 100-meter all-glass baseline wind turbine blades (SNL 100–00) (Griffith and Ashwill 2011). The length of each blade is 100 m, the overall structure height (when one blade is resting at its top vertical position, see Fig. 5.12) is 250 m, and the distance from the leader tip to the ground is $z_0 = 250$ m. The length of the lightning stepped leader is 3750 m. The distance from the ground to the cloud is 4000 m. Moreover, a typical 100 m non-conductive wind turbine blade is equipped with multiple receptors, which are evenly embedded on each side of the blade surface and are connected to the internal down conductor (e.g., unshielded high-voltage cables that are installed inside the blade shell extending from the blade tip to the root buildup, see Fig. 5.5). In this finite element model, the effects of the receptors and the down conductors are taken into account through applying ground potential boundary conditions to the surface of the wind turbine blades. In addition, it is assumed that the lightning stepped leader is a vertical line charge that is perpendicular to the turbine axis and is located in the same plane with the blades (see Fig. 5.12). Moreover, since blades are 100-meter long, the rolling sphere method is used to obtain the lightning strike distance (i.e., d in Fig. 5.12). It is assumed that the rolling sphere is tangentially attached to the tip of the blade OA. The lightning striking distance between the leader and blade OA is equal to the rolling sphere radius Eq. (5.1). Here, the attachment to the tip is chosen because the tip region of the blade has the highest probability (>98%) to emit answering leaders (Madsen 2006).

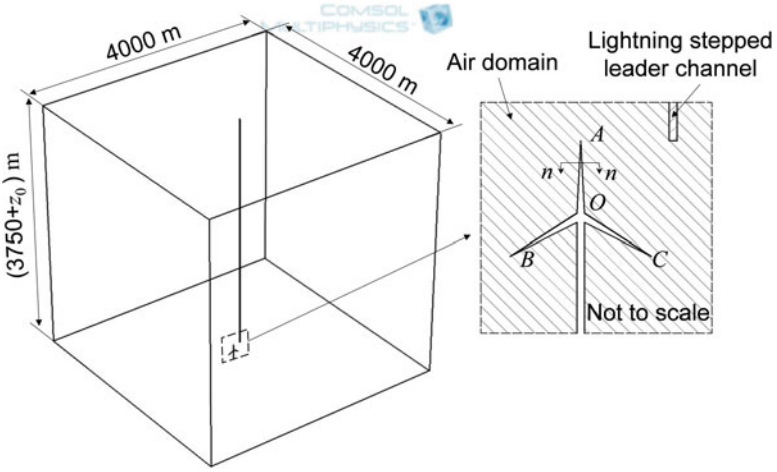

Fig. 5.13 Problem setup in COMSOL

The computational domain is a 3D parallelepiped containing a cutout in the shape of a wind turbine as shown in Fig. 5.13. The dimensions of the cutout are determined by the dimensions of the wind turbine. To simplify the problem, the wind turbine blades are assumed to be beams of square cross section, 2.5 m by 2.5 m. The computational domain represents the air between a cloud and the ground. The length and width of the parallelepiped are 4000 m. The depth is $L + z_0$, where $L = 3750$ m is the length of the lightning stepped leader and $z_0 = 250$ m is the distance from the tip of the leader to the ground. The lightning stepped leader is assumed to be a vertical cylindrical channel of length $L = 3750$ m and radius $R_l = 5$ m. The cylindrical leader channel is placed in the center of the 3D parallelepiped extending from the top surface to the bottom surface (see Fig. 5.13). A volume charge density, $\rho_v = \lambda/\pi R l^2$, where λ is the line charge density Eq. (5.9), is applied to the leader channel. The lightning striking distance, d, as shown in Fig. 5.12, is calculated using the rolling sphere radius Eq. (5.1).

In addition, an electric potential, $V = 40$ MV (Becerra 2008), representing the cloud voltage, is applied to the top surface of the parallelepiped. Ground potential is applied to the bottom surface of the parallelepiped and to the exterior surface of the wind turbine (i.e., hub, nacelle, and the tower) and the surface of the three wind turbine blades (i.e., to account for the effects of multiple receptors and down conductors). Open boundary conditions are assumed at all four vertical sides of the parallelepiped. Moreover, the domain (including the leader) is assigned with an "air material" defined in the COMSOL Material Library. The domain is meshed with 815,112 free tetrahedral elements. The average duration of each simulation is 128 s on a four-core laptop PC.

Next, FEA was performed to predict the electric fields along the wind turbine blades *OA*, *OB*, and *OC* (see Fig. 5.13). FEA results are shown in Table 5.3 and

Table 5.3 The magnitude of the electric field at the wind turbine blade tips and the stepped leader tip (nonuniform charged lightning stepped leader, $z_0 = 250$ m)

Magnitude of the electric field (V/m)			
Blade *OA* tip	Blade *OB* tip	Blade *OC* tip	Lightning stepped leader tip
$1.60 \cdot 10^7$	$5.30 \cdot 10^6$	$6.05 \cdot 10^6$	$2.09 \cdot 10^7$

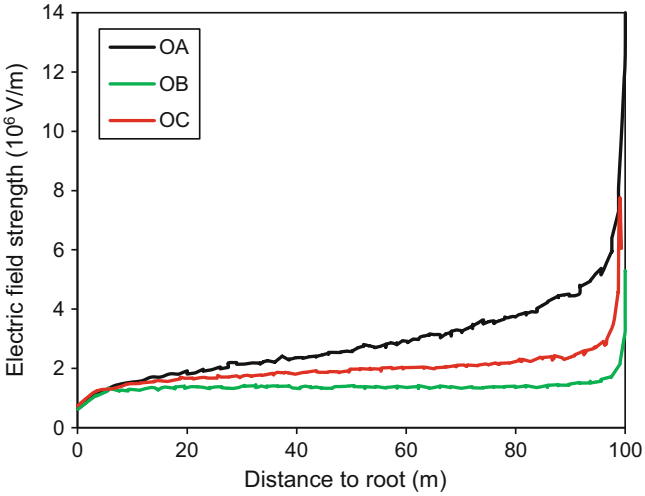

Fig. 5.14 The magnitude of the electric field at blades *OA*, *OB*, *OC*, LPL I

Figs. 5.14 and 5.15. Figure 5.14 shows the electric field strength along the blades *OA*, *OB*, and *OC* at LPL I (i.e., $I_{peak} = 200$ kA). It can be seen that the electric field at blade *OA* is larger than that at blades *OB* and *OC*. However, although the peak current corresponding to LPL I is the highest comparing to the less severe conditions (i.e., LPL II and LPL III), the electric field strength at the tip of blade *OA* could be considerably lower than those obtained under LPL II and LPL III conditions (Wang and Zhupanska 2014). Lastly, Fig. 5.15 shows a contour plot of the electric field strength distribution in the vicinity of the wind turbine.

It is worth emphasizing again that the effect of the dynamic propagation of the lightning stepped leader was not taken into account in the above calculations. In other words, only the static electric field was predicted at the particular moment when the lightning stepped leader arrived within the lightning striking distance. Future simulations are suggested to incorporate the effect of dynamic propagation of the lightning stepped leader for a more accurate prediction of electric field and therefore a more accurate estimation of dielectric breakdown in the composite structures (see discussion in Sect. 5.2.4).

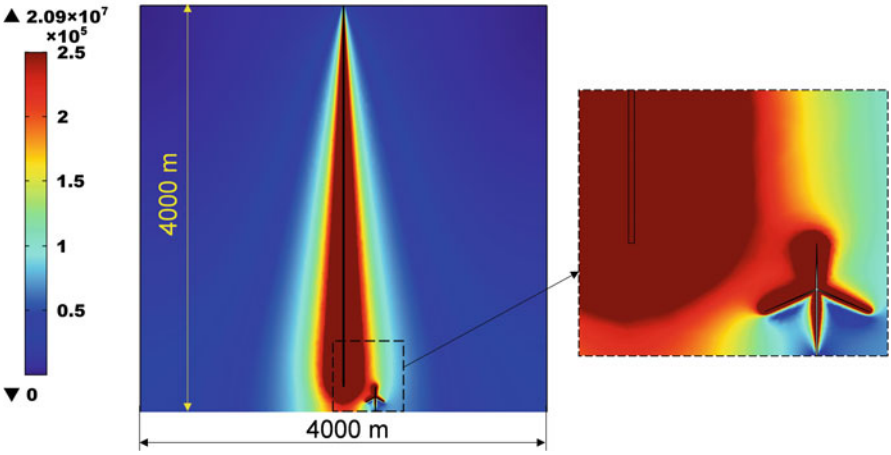

Fig. 5.15 Electric field magnitude distribution in the vicinity of the wind turbine at LPL I

5.2.4 Estimation of Dielectric Breakdown of Non-conductive Composite Wind Turbine Blades

As described in Sect. 5.1.2, severe lightning strikes may cause the dielectric breakdown of the non-conductive composite wind turbine blade, which could lead to punctures through the thickness direction of the blade and even more extensive structural damage. Therefore, it is quite crucial to evaluate the conservativeness of the blade design against the lightning strike-induced dielectric breakdown. A straightforward method for such evaluation is to compare the predicted electric field strength (see Sect. 5.2.3) with the dielectric breakdown strength of the wind turbine blade. If the dielectric breakdown strength of the blade is lower than the predicted electric field strength on the blade induced by the lightning strike, the blade is very likely to experience dielectric breakdown. The previous section (Sect. 5.2.3) describes the methods to predict the electric field strength in the vicinity of the wind turbines due to lightning strikes. In this section, we provide some discussions on the dielectric breakdown strength of composite wind turbine blades.

Experimental investigations (Madsen et al. 2004, 2006) on the dielectric breakdown strength of the glass fiber polymer-matrix (GFRP) composite laminates used on the wind turbine blades revealed that the dielectric breakdown strength is a function of both the thickness and the surface tracking resistance of the composites and is expressed by

$$E_b = a/t + b \cdot TI, \tag{5.14}$$

where E_b is the average dielectric breakdown strength (V/m), a and b are the coefficients, t is the thickness of the composite laminate (m), and TI is the tracking

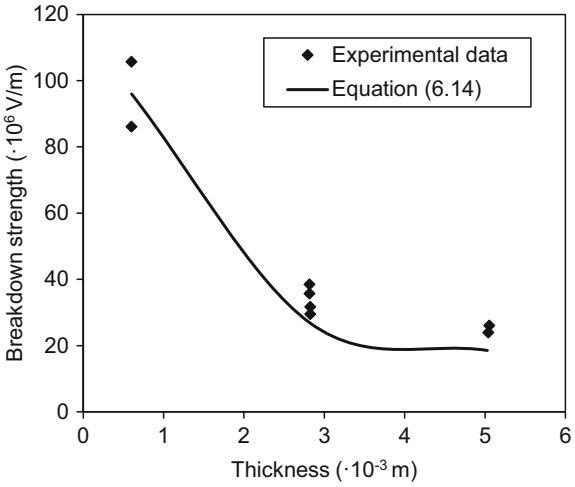

Fig. 5.16 Dielectric breakdown strength of the GFRP composite laminate

index, which is highly dependent on the fiber orientation, fiber and matrix properties, surface defects, and wide erosions. Generally, the values of the tracking index are stochastic due to uncertainties involved in manufacturing and handling (Madsen 2006; Madsen et al. 2004, 2006). Here, the product of the coefficient b and the tracking index is assumed to be a constant, i.e., $b{\cdot}TI = 8.0{\cdot}10^6$. The coefficient a is $5.3{\cdot}10^4$. These parameters were chosen by fitting the experimental data reported by (Madsen 2006, Madsen et al. 2004, 2006). Figure 5.16 shows the comparison between the dielectric breakdown strength that is predicted using Eq. (5.14) and the dielectric breakdown strength obtained from experimental tests (Madsen 2006; Madsen et al. 2004, 2006). It should be mentioned that the dielectric breakdown strength of the GFRP composite laminate reported by Madsen (2006), Madsen et al. (2004, 2006) is for laminates with thicknesses within 2∼6 mm. However, in practical situations, the laminate thickness of the real blades can reach to ∼100 mm. The applicability of Eq. (5.14) to describe the dependence of dielectric breakdown on the thickness may be questioned and needs further investigation.

Meanwhile, according to the ASTM standard (ASTM 1994), the breakdown strength for solid can be expressed by

$$E_b = 4.2/t + 63/\varepsilon_s, \tag{5.15}$$

where ε_s is the permittivity of the solid. From Eq. (5.15), it can be seen that, in cases of large thickness and low permittivity (∼4 for GFRP according to (Madsen 2006; Madsen et al. 2004, 2006) specimens, the term containing t becomes relatively insignificant, and the product of permittivity and the breakdown strength are approximately a constant. In other words, the dielectric breakdown strength approximately becomes a constant (∼15 MV/m) when the thickness increases. The same can be captured by Eq. (5.14). Therefore, here, we assume that Eq. (5.14) can be extrapolated to describe the thickness dependence on the dielectric breakdown of the wind turbine blade along the entire spanwise, for which the thickness may

Fig. 5.17 Planform of Sandia 100-m baseline blade with laminated designations (Blue, spar cap; orange, trailing edge reinforcement; red, additional shear web) (Griffith and Ashwill 2011)

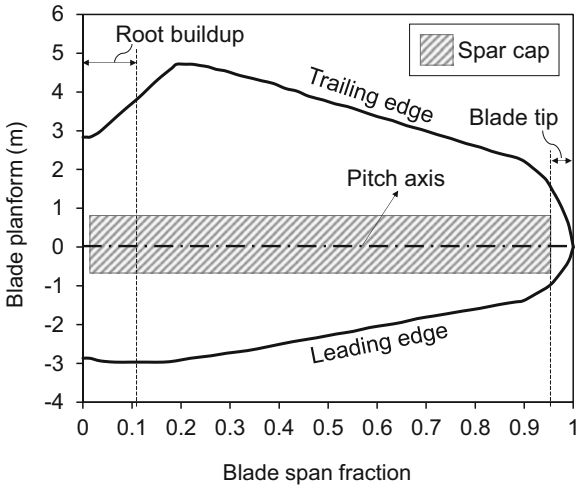

Fig. 5.18 Sandia 100-meter all-glass baseline wind turbine blade (SNL 100–00) planform

be larger than 6 mm. Note that this extrapolation may not be rigorous due to the lack of experimental data. If more experimental data are available, a more accurate expression to describe the thickness dependence on the dielectric breakdown can be found.

Now we present an example to estimate the dielectric breakdown strength of a wind turbine blade. This particular blade considered here is the Sandia 100-meter all-glass baseline wind turbine blade (SNL 100–00) (Griffith and Ashwill 2011). The planform of the blade is shown in Figs. 5.17 and 5.18.

The root buildup and spar cap of the blade are made of GFRP composites. The other parts of the blade are made of sandwich panels with foam core and GFRP composite facesheets. The experimental data on the dielectric breakdown strength of the sandwich composites are not available, so only the root buildup and spar cap sections are considered. Moreover, the blade is divided into 34 sections along the spanwise direction. Thicknesses of the root buildup and spar cap at various sections along the spanwise direction are shown in Table 5.4. The dielectric breakdown strengths of the root buildup and spar cap along the spanwise direction are calculated using Eq. (5.14) and shown in Fig. 5.19. Then, they are compared to the magnitudes of the predicted electric fields along the blade *OA* obtained using FEA (see Sect. 5.2.3). The ratios of the dielectric breakdown strength to the magnitude of the predicted electric field (referred to "safety factor" hereinafter) are shown in Fig. 5.20. As one can see, the root buildup design is generally conservative against the dielectric breakdown, for which the safety factor is far above 1, whereas

Table 5.4 Composite laminate thickness at various sections of the wind turbine blade (Griffith and Ashwill 2011)

Section number	Blade span fraction	Overall thickness (mm)	
		Root buildup	Spar cap
1	0.000	170	
2	0.005	150	1
3	0.007	130	2
4	0.009	110	3
5	0.011	90	4
6	0.013	80	10
7	0.024	73	13
8	0.026	65	13
9	0.047	50	20
10	0.068	35	30
11	0.089	25	51
12	0.114	15	68
13	0.146		94
14	0.163		111
15	0.179		119
16	0.195		136
17	0.222		136
18	0.249		136
19	0.277		128
20	0.358		119
21	0.439		111
22	0.521		102
23	0.602		85
24	0.667		68
25	0.683		64
26	0.732		47
27	0.765		34
28	0.846		17
29	0.895		9
30	0.944		5
31	0.957		5
32	0.972		5
33	0.986		5
34	1.000		

the tip region is comparatively less conservative, for which the safety factor is only 1.55. This low safety factor 1.55 indicates that the tip of blade *OA* has the highest risk of experiencing dielectric breakdown. Recall that electric fields along blades *OB* and *OC* are generally weaker than those along blade *OA*. Overall, blade *OA* is the most vulnerable one to the dielectric breakdown.

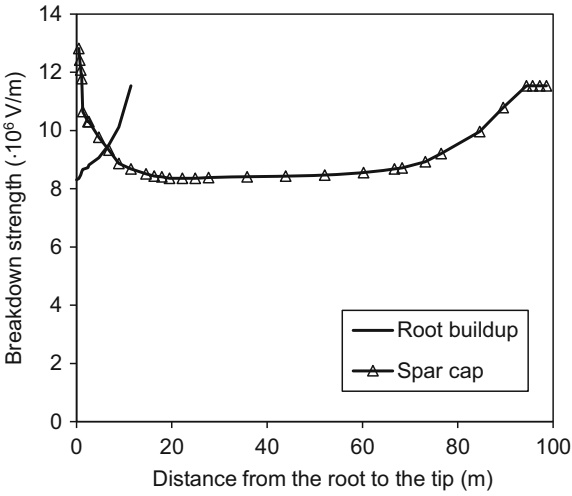

Fig. 5.19 Dielectric breakdown strength of the Sandia 100-meter all-glass baseline wind turbine blade (SNL 100–00) at both root buildup region and spar cap region. Distance at 0 denotes the blade root and distance at 100 m denotes the blade tip

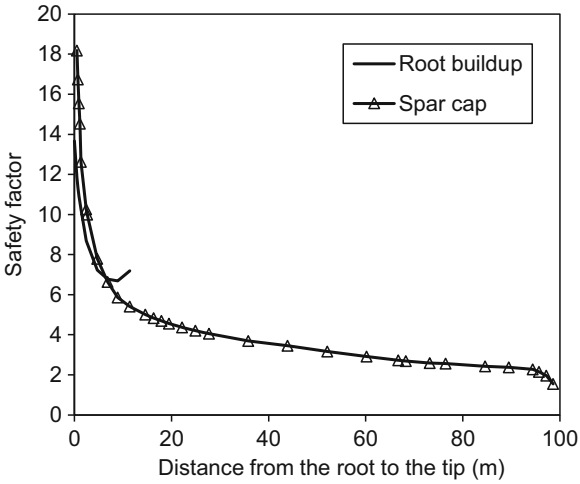

Fig. 5.20 Safety factor (ratio between estimated dielectric breakdown strength and electric field predicted) at LPL I for wind turbine blade *OA* root buildup region and spar cap region

It is worth mentioning that the dielectric breakdown strength of the composite materials may deteriorate during the service lifetime of wind turbine blades due to the presence of moisture, defect accumulation, etc. Although experimental data specific to composite wind turbine blades are not available, laboratory studies of glass-reinforced composites may be useful to assess the extent of deterioration in properties. For instance, experimental results reported by Morgan et al. (2009) indicate that cyanate ester/S2 glass composite retains 90% of its dielectric strength after 6-month exposure to 99% humidity. Hong et al. (2009) observed that the breakdown strength of the specimens underwent a 67% reduction when the dry specimen was immersed in water until their weight was increased by 1.5%.

5.3 Current Predictive Models of Lightning Strike-Induced Thermal and Ablative Damage in Non-conductive Composite Wind Turbine Blades

In the case when the dielectric breakdown does not occur in composite laminated blades, lightning strike attachments will come as a direct heat injection into the surface of the non-conductive blades. The direct heat injection can produce a considerable damage that includes thermal ablation, internal explosion, and delamination.

As a part of damage prediction due to lightning-induced heat injection, a heat transfer problem needs to be solved (Wang and Zhupanska 2015). A heat transfer problem formulation for non-conductive structures (e.g., GFRP composite wind turbine blades) is different from the one for conductive structures (e.g., carbon fiber-reinforced polymer-matrix (CFRP) composite wind turbine blades). For the conductive structures, a heat transfer equation has to be solved simultaneously with electrodynamics equations to determine the distribution of the electric current and associated Joule heat densities. In the following sections, the formulation of such heat transfer problem is provided, along with brief descriptions on the estimation of different structural damage (i.e., delamination and thermal ablation) using the obtained heat distributions.

5.3.1 Heat Transfer Due to Lightning Strike Current

The attachment of the lightning arc onto the surface of the wind turbine blade (i.e., laminated and sandwiched composite structures with possible coatings) produces considerable heat. The heat conduction in the material is governed by the energy balance equation. To account for the electric-thermal coupling effects (if the composite material is electrically conductive, such as the CFRP composites), the energy balance equation is written as (Abdelal and Murphy 2014; Muñoz et al. 2014; Ogasawara et al. 2010; Wang et al. 2014; Wang and Zhupanska 2014, 2016)

$$\rho C_p \left(\frac{\partial T}{\partial t} - \dot{s} \frac{\partial T}{\partial z} \right) = \nabla \cdot (\mathbf{k} \nabla T) + Q_J + Q_L, \tag{5.16}$$

where ρ, C_p, and $\mathbf{k}$ are, respectively, the instant density, specific heat, and directional thermal conductivity of the composite material, all of which are temperature dependent, $\dot{s}$ is the surface recession rate due to progressive material removal (e.g., rapid vaporization), z is the coordinate normal to the material surface, Q_J is internal Joule heating generation, $Q_J = \mathbf{J} \cdot \mathbf{E}$ (where $\mathbf{J}$ is the lightning current density and $\mathbf{E}$ is the electric field), and Q_L is the energy loss due to the resin decomposition (i.e., liberation of pyrolysis gases).

Meanwhile, the current density is governed by the Ohm's law:

$$\mathbf{J} = \boldsymbol{\sigma} \cdot \mathbf{E}, \tag{5.17}$$

where $\boldsymbol{\sigma}$ is the temperature-dependent electrical conductivity tensor.

The energy loss, Q_L, is mainly due to the liberation of the pyrolysis gases, for which the induced pyrolysis gases percolate through the material to the surface and bring part of the heat away. The energy loss is highly dependent on the density variation of the material during the heating process, the enthalpy of the material, and the enthalpy of the pyrolysis gases. Parameters such as the density variation of the material during the heating process are usually determined using thermogravimetric (TGA) tests. However, such tests are normally conducted under the laboratory conditions for which the heating rates applied to the materials were normally lower than 50 °C/min (Feih and Mouritz 2012; Negarestani et al. 2010; Ogasawara et al. 2002). Such low heating rate cannot represent the lightning strike conditions, since the heating rate under lightning strike conditions can reach $\sim 10^{10}$ °C/min. Many experimental evidences (Feih and Mouritz 2012; Negarestani et al. 2010; Ogasawara et al. 2002) have shown that the mass loss under high heating rate is much lower than that under low heating rate when temperature rises to the same magnitude. Therefore, under lightning strike conditions, it is expected that the mass loss rate is significantly lower than the mass loss rates obtained in those traditional TGA tests. To the author's knowledge, TGA experimental tests under lightning strike conditions have not been reported. The author hereby suggests the experimentalists to develop techniques to enable future TGA tests with the capability of applying extreme high heating rates or to develop alternative experimental tests.

In addition to the difficulties in determining the density variations during the lightning strike heating process, the accurate determination of the material parameters (i.e., directional thermal/electric conductivity, specific heat) from room temperature to the sublimation temperature of the glass/carbon fiber is still quite a challenging task to date.

5.3.2 Thermal Ablation

The ablation mechanism of the fiber-reinforced polymer-matrix composite material (i.e., the material used for wind turbine blades) due to lightning strike is extremely complicated and is still not well understood to date. One should not confuse lightning strike-induced ablation with pulsed laser ablations, although both of them induce rapid heating in the solid materials. The particle composition of lightning arc and the laser beam is quite different (i.e., photons for laser and electrons for lightning arc). Furthermore, materials (e.g., copper, aluminum) are reported to experience phase explosions if subjected to high fluence pulsed laser beam injection (Bulgakova and Bulgakov 2001; Gragossian et al. 2009; Wang et al. 2017). However, phase explosion has never been reported in the literature on lightning strike damage investigations.

The ablation mechanisms of the composite materials are strongly related to the phase transition of the material. For non-conductive GFRP composite materials, the mass loss comes from the decomposition of the resin (300 °C ∼ 800 °C) and the rapid vaporization of the melted glass fiber (∼1100 °C) (Dec et al. 2012). For electrically conductive CFRP composites, the ablation mechanism is more complicated. Under elevated temperatures, resin decomposes; meanwhile, carbon atoms in the carbon fibers react with gas species O, C, and H in the air which leads to a rapid mass loss. These reactions include oxidation, nitridation, and sublimation. It appears that the most significant mass loss of CFRP composites is attributed to the sublimation reaction, since the mass loss rates due to oxidation and nitridation reactions are normally much lower. Further experimental investigations are needed to provide more insights into the effects of these reactions on the total mass loss of the composite materials under lightning strike conditions. In addition to these surface-gas reactions, the flow of electric current inside the CFRP composite structure also leads to the generation of internal Joule heating and may lead to additional volumetric mass loss.

5.3.3 Delamination

Delamination is also another commonly reported damage form of the wind turbine blades after lightning strikes. Existing lightning strike experimental studies (Feraboli and Kawakami 2010; Feraboli and Miller 2009; Hirano et al, 2010; Li et al. 2015) examined the damage in the composite material specimens subjected to the artificial pulsed lightning current (components A or D of the standard lightning current waveform (MIL-464-A 1997), see Fig. 5.1) and have identified that delamination (i.e., interlaminar damage) is the most significant damage. Ogasawara et al. (2010) was the first to predict the lightning strike delamination in CFRP composites with a coupled electric-thermal FEA. The material area where the temperature is above the resin decomposition threshold temperature (∼300 °C) was assumed to be the delamination area. However, no actual continuum delamination modeling was accomplished. In addition, the lightning strike-induced shockwave pressure (i.e., acoustic and magnetic), which is the primary cause of delamination, was not taken into account in this model. Muñoz et al. (2014) predicted the stress-induced damage of a CFRP composite panel under the action of the electromagnetic and acoustic pressure. However, continuum delamination was also not captured. Recently, a more sophisticated model was proposed by P. Naghipour et al. (2016), which enabled us to capture the continuum lightning strike delamination using the cohesive zone approach with FEA. In this section, the cohesive zone approach for modeling delamination is briefly reviewed and discussed.

The cohesive zone approach lends itself naturally to the modeling of continuum delamination in laminated composite structures. To use the approach, the laminated composite structure is typically modeled at the ply level, which means the laminate plies are modeled as individual elastic, homogenous transversely isotropic plies, and

the interface of the plies (i.e., resin layers) is modeled with interface elements (i.e., cohesive elements in ABAQUS) with zero thickness.

The damage initiation criterion of the cohesive element used in Naghipour et al. (2016) is the quadratic interfacial traction interaction criterion:

$$\left(\frac{\tau_n}{\tau_n^0(T)}\right)^2 + \left(\frac{\tau_s}{\tau_s^0(T)}\right)^2 + \left(\frac{\tau_t}{\tau_t^0(T)}\right)^2 = 1, \tag{5.18}$$

where τ is the interfacial traction, τ^0 is the temperature-dependent interfacial elastic traction limits, and subscripts n, s, and t denote the normal direction and two shear directions, respectively. The interfacial traction τ can be calculated using the interfacial constitutive relationship:

$$\tau = \mathbf{D}\delta, \tag{5.19}$$

where δ is the relative displacement between the upper and bottom nodes of each cohesive element and $\mathbf{D}$ is the interfacial constitutive secant tensor (Naghipour et al. 2011).

At each time increment, the interfacial traction τ is calculated using Eq. (5.19) and is plugged into Eq. (5.18) to check whether damage is initiated. If damage is initiated (δ_m^0 is the relative displacement corresponding to damage initiation in Fig. 5.21), the propagation of the damage follows the Benzeggagh and Kenane (B-K) criterion:

$$G_{IC}(T) + (G_{IIC}(T) - G_{IC}(T))\left(\frac{m^2}{1+m^2}\right)^{\eta} = G_C(T), \tag{5.20}$$

where $G_{IC}(T)$ and $G_{IIC}(T)$ are the temperature-dependent fracture toughness values for mode I and mode II, respectively; m is the mode mixty (Naghipour et al. 2011); and η is a parameter related to the shape of the failure locus in the mixed mode plane.

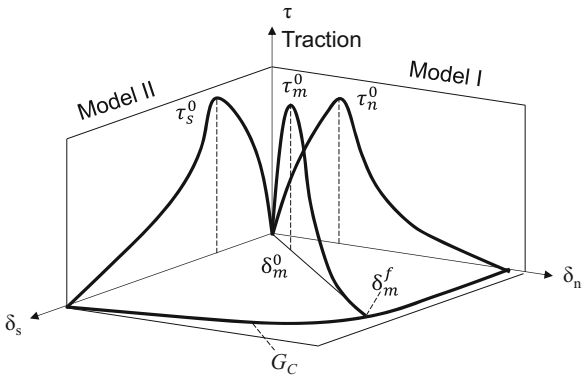

Fig. 5.21 Schematic of mixed mode traction separation law for cohesive elements

The implementation of the cohesive zone approach can be achieved in commercial FEA software, such as ABAQUS using the build-in cohesive elements. The parameters of the damage initiation Eq. (5.18) and propagation Eq. (5.20) criterions of the cohesive elements can be defined in the ABAQUS input file. Meanwhile, ABAQUS allows the cohesive elements to be progressively deleted when the final separation point (δ_m^f in Fig. 5.21) is reached; as such, the continuum delamination of the laminated composite structure can be captured.

5.4 Conclusions and Future Recommendations

5.4.1 Conclusions

In this chapter, the basic physics of lightning strike and the interaction between the lightning strike and the wind turbine are discussed. The key mechanisms of the lightning strike damage on the wind turbine blades and the commonly used lightning strike protections are introduced. In addition, the mechanisms of lightning current conduction through the non-conductive GFRP composite wind turbine blade are discussed. Furthermore, the analytical and finite element methods of predicting the lightning strike-induced electric field in the vicinity of a wind turbine are demonstrated. The predicted electric fields are used to compare with the dielectric breakdown strength of the GFRP composite wind turbine blade to estimate the conservativeness of the blade design against lightning strike dielectric breakdown. Moreover, other forms of lightning damage for wind turbine blades are introduced including the thermal ablation and delamination. The corresponding damage mechanisms and their mathematical formulations have been presented.

5.4.2 Future Recommendations

For future study on the lightning strike analysis of wind turbines, there is a need to incorporate the effects of dynamic propagation of the lightning stepped leader into the analysis of the lightning strike-induced electric fields, such that a more accurate estimation of dielectric breakdown in the composite wind turbine blades can be achieved. In addition, there is a need to develop improved lightning thermal and damage models that include the accurate determination of the temperature-dependent thermophysical properties and the mass loss rate of the composite materials under lightning strike conditions, as well as the proper treatment for material phase transitions during the numerical implementation. Furthermore, it should be mentioned that the current lightning damage models in the literature

restrict their analyses to a single type of lightning damage. However, in practical situations, the three lightning damage mechanisms (i.e., ablation, delamination, and dielectric breakdown) may occur at the same time. Hence, the challenge for future research is to develop a fully coupled damage model that concurrently performs all of the three lightning damage analyses.

References

Abdelal G, Murphy A (2014) Nonlinear numerical modelling of lightning strike effect on composite panels with temperature dependent material properties. Compos Struct 109:268–278. Elsevier

ASTM (1994) Standard test method for dielectric breakdown voltage and dielectric strength of solid electrical insulating materials at commercial power frequencies. Retrieved from Technical Report, West Conshohocken

Becerra M (2008) On the attachment of lightning flashes to grounded structures. PhD, Acta Universitatis Upsaliensis

Bulgakova NM, Bulgakov AV (2001) Pulsed laser ablation of solids: transition from normal vaporization to phase explosion. Appl Phys A Mater Sci Process 73(2):199–208

Chemartin L, Lalande P, Peyrou B, Chazottes A, Elias PQ, Delalondre C, Cheron BG, Lago F (2012) Direct effects of lightning on aircraft structure: analysis of the thermal, electrical and mechanical constraints. AerospaceLab 5:1

Cooray V, Rakov V, Theethayi N (2007) The lightning striking distance—revisited. J Electrost 65(5):296–306

D'Alessandro F, Petrov NI (2006) Field study on the interception efficiency of lightning protection systems and comparison with models. In: Proceedings of the Royal Society of London A: Mathematical, Physical and Engineering Sciences. The Royal Society 462(2069): 1365–1386

Dec JA, Braun RD, Lamb B (2012) Ablative thermal response analysis using the finite element method. J Thermophys Heat Transf 26:201–212

Eriksson AJ (1979) The lightning ground flash: an engineering study. PhD, University of KwaZulu-Natal, Durban

Feih S, Mouritz AP (2012) Tensile properties of carbon Fibres and carbon fibre–polymer composites in fire. Compos A: Appl Sci Manuf 43:765–772. Elsevier

Feraboli P, Kawakami H (2010) Damage of carbon/epoxy composite plates subjected to mechanical impact and simulated lightning. J Aircr 47:999–1012

Feraboli P, Miller M (2009) Damage resistance and tolerance of carbon/epoxy composite coupons subjected to simulated lightning strike. Compos A: Appl Sci Manuf 40:954–967. Elsevier

Golde RH (1945) The frequency of occurrence and the distribution of lightning flashes to transmission lines. Electr Eng 64(12):902–910

Golde RH (1977) Lightning. Academic Press, London

Gragossian A, Tavassoli SH, Shokri B (2009) Laser ablation of aluminum from normal evaporation to phase explosion. J Appl Phys 105(10):103304

Griffith DT, Ashwill TD (2011) The Sandia 100-meter all-glass baseline wind turbine blade: SNL100–00. Sandia National Laboratories, Albuquerque. SAND2011–3779

Hirano Y, Katsumata S, Iwahori Y, Todoroki A (2010) Artificial lightning testing on graphite/epoxy composite laminate. Compos A: Appl Sci Manuf 41:1461–1470. Elsevier

Hong TP, Lesaint O, Gonon P (2009) Water absorption in a glass-mica-epoxy composite-[I: influence on electrical properties]. Dielectr Electr Insul IEEE Trans 16(1):1–10

IEC-61400-24 (2002) Wind turbine generator systems–part 24: lightning protection. International Electrotechnical Commission, Geneva

Inoue K, Korematsu Y, Nakamura N, Matsushita T, Murata N, Kuroiwa T, Shibata M, Ueda Y, Arinaga S, Suguro Y (2004) Study on damage-mechanism of wind turbine blades by lightning strike. Paper presented at the international conference on lightning protection, Avignon

Lewke B, Hernández YM, Kindersberger J (2007) A simulation method for the wind turbine's electric field distribution caused by the stepped lightning leader. Paper presented at the European wind energy conference, 9 May

Li Y, Li R, Lu L, Huang X (2015) Experimental study of damage characteristics of carbon woven fabric/epoxy laminates subjected to lightning strike. Compos A: Appl Sci Manuf 79:164–175. Elsevier

Madsen SF (2006) Interaction between electrical discharges and materials for wind turbine blades-particularly related to lightning protection. PhD, Technical University of Denmark

Madsen SF, Holbøll J, Henriksen M, Larsen FM, Hansen LB, Bertelsen K (2004) Breakdown tests of glass fibre reinforced polymers (GFRP) as part of improved lightning protection of wind turbine blades. Paper presented at the IEEE international symposium on electrical insulation, Indianapolis, 19–22 September

Madsen SF, Holboll J, Henriksen M (2006) Direct relationship between breakdown strength and tracking index of composites. Paper presented at the IEEE international symposium on electrical insulation, Toronto, 11–14 June

MIL-464-A (1997) Electromagnetic environmental effects requirements for systems. US Department of Defense, Washington, DC

Morgan B, Madhukar M, Walsh J, Hooker M, Grandlienard S (2009) Moisture degradation of cyanate ester/S2 glass composite insulation systems. J Compos Mater 44:821–837

Muñoz R, Delgado S, González C, López-Romano B, Wang D-Y, Llorca J (2014) Modeling lightning impact thermo-mechanical damage on composite materials. Appl Compos Mater 21:149–164. Springer Netherlands

Naghipour P, Bartsch M, Voggenreiter H (2011) Simulation and experimental validation of mixed mode delamination in multidirectional CF/PEEK laminates under fatigue loading. Int J Solids Struct 48(6):1070–1081

Naghipour P, Pineda EJ, Arnold SM (2016) Simulation of lightning-induced delamination in unprotected CFRP laminates. Applied Composite Materials 23(4):523–535

Negarestani R, Li L, Sezer HK, Whitehead D, Methven J (2010) Nano-second pulsed DPSS Nd: YAG laser cutting of CFRP composites with mixed reactive and inert gases. Int J Adv Manuf Technol 49:553–566. Springer

Oard M (2015) The new weather book. New Leaf Publishing Group, Incorporated, Green Forest

Ogasawara T, Ishikawa T, Yamada T, Yokota R, Itoh M, Nogi S (2002) Thermal response and ablation characteristics of carbon Fiber reinforced composite with novel silicon containing polymer MSP. J Compos Mater 36:143–157. Sage Publications

Ogasawara T, Hirano Y, Yoshimura A (2010) Coupled thermal–electrical analysis for carbon Fiber/epoxy composites exposed to simulated lightning current. Compos A: Appl Sci Manuf 41:973–981. Elsevier

Rupke E (2002) Lightning direct effects handbook. Lightning Technologies Inc. Report No. AGATE-WP3, 1-031027. Retrieved from: http://www.niar.wichita.edu/agate/Documents/Lightning/WP3.1-031027-043.pdf

Tipler PA, Mosca G (2007) Physics for scientists and engineers. Macmillan, New York

Uman MA (2001) The Lightning Discharge, 2nd edn. Dover Publications Inc., New York

Wang Y, Hu W (2017) Investigation of the effects of receptors on the lightning strike protection of wind turbine blades. IEEE Trans Electromagn Compat 59(4):1180–1187

Wang Y, Zhupanska OI (2014) Evaluation of the thermal damage in glass fiber polymer-matrix composites in wind turbine blades subjected to lightning strike. Paper presented at the American Society for Composites 29th annual technical conference, San Diego, 8–10 September

Wang Y, Zhupanska OI (2015) Lightning strike thermal damage model for glass Fiber reinforced polymer matrix composites and its application to wind turbine blades. Compos Struct 132:1182–1191. Elsevier

Wang Y, Zhupanska OI (2016) Thermal ablation in fiber-reinforced composite laminates subjected to continuing lightning current. Paper presented at the 57th AIAA/ASCE/AHS/ASC structures, structural dynamics, and materials conference, San Diego

Wang FS, Ding N, Liu ZQ, Ji YY, Yue ZF (2014) Ablation damage characteristic and residual strength prediction of carbon Fiber/epoxy composite suffered from lightning strike. Compos Struct 117:222–233. Elsevier

Wang Y, Shen N, Befekadu GK, Pasiliao CL (2017) Modeling pulsed laser ablation of aluminum with finite element analysis considering material moving front. Int J Heat Mass Transf 113:1246–1253